Imaging the global solar wind flow in EUV

Mike Gruntman,[1] Vlad Izmodenov,[2,3] and Vic Pizzo[4]

Received 13 November 2005; revised 5 January 2006; accepted 18 January 2006; published 22 April 2006.

[1] We advance the original concept of imaging the three-dimensional solar wind flow (Gruntman, 2001a) by characterizing expected heliospheric EUV signatures under assumptions of a realistic solar wind. Charge exchange collisions between the solar wind alpha particles and heliospheric atomic hydrogen produce unique emissions in the 30.4-nm line. All-sky images at 30.4 nm with high spectral resolution reveal the three-dimensional flow properties of the solar wind, including the flow in the regions over the Sun's poles, and the variability of the global solar wind properties during the 11-year solar cycle. We simulate global heliospheric images at 30.4 nm for a realistic three-dimensional solar wind with the Sun's effective magnetic dipole tilted with respect to the spin axis, resulting in a complex flow pattern of the plasma. We show that the physical properties of the flow would permit averaging over several rotations of the Sun, thus realistically limiting the total number of all-sky images to a few per year. This feature effectively establishes the sensitivity requirements for an experiment to image the global solar wind.

Citation: Gruntman, M., V. Izmodenov, and V. Pizzo (2006), Imaging the global solar wind flow in EUV, *J. Geophys. Res.*, *111*, A04216, doi:10.1029/2005JA011530.

1. Three-Dimensional Heliosphere in EUV

[2] The solar wind flow is essentially three-dimensional and its anisotropy significantly varies during the 11-year solar cycle. At solar minimum the polar solar wind plasma is faster and less dense than the low-latitude (heliolatitude) solar wind within ±20° from the equator, as directly measured by the Ulysses spacecraft [e.g., *Neugebauer*, 1999; *McComas et al.*, 2000]. Anisotropy diminishes during solar maximum, with the solar wind flow pattern exhibiting a complex structure [*McComas et al.*, 2003]. When and how does the global flow change during the cycle? Is this change symmetric with respect to heliographic latitude and heliographic longitude? What are the timescales of the change? These questions are unanswered.

[3] The unique in situ observations of the solar wind from a single out-of-ecliptic spacecraft such as Ulysses are so sparse that they make anything more than an initial step in understanding of the average global configuration of the solar wind impossible. Single-point measurements do not separate important temporal and spatial variations in the solar wind. In addition, propulsion limitations will confine most space missions to the ecliptic plane for many years. Consequently, characterization of an essentially three-dimensional and time-varying flow pattern of the solar wind requires remote techniques to complement Ulysses-type "ground truth" in situ measurements. The recently proposed [*Gruntman*, 2001a] new concept to remotely probe the global solar wind flow is based on unique emissions of the solar wind plasmas in extreme ultraviolet (EUV).

[4] Charge exchange collisions between the solar wind alpha particles (He^{2+}) and heliospheric atomic hydrogen (H) produce unique emissions in the 30.4-nm line (the resonance transition in He^{+}). The areas of the sky with the higher solar wind velocity would stand out in brightness because of the velocity dependence of charge-exchange cross sections. In addition, solar wind velocities can be directly determined from Doppler shifts [*Gruntman*, 2001a]. Other sources of diffuse radiation in the heliosphere at 30.4 nm, with radiances similar to that of the solar wind emissions, include emissions of hot plasmas in the Local Bubble and the glow of (scattering of the solar line emission by) He^{+} ions in interstellar plasma flowing around the heliopause and the glow of He^{+} pickup ions in the solar wind. It is important that the solar wind emissions are spectrally separated (owing to Doppler shifts) from these other sources of diffuse radiation, which opens a way of probing the three-dimensional solar wind flow remotely [*Gruntman*, 2001a, 2001b].

[5] Remote probing of the solar wind flow constitutes integral part of global heliosphere imaging in EUV, a concept that also aims at exploring remotely the properties of the boundary separating the solar wind and galactic plasmas, the heliopause, and magnetic field and the ionization state and flow field of interstellar plasma beyond [*Gruntman*, 2001a, 2001b, 2005; *Gruntman et al.*, 2005].

[1]Astronautics and Space Technology Division, Viterbi School of Engineering, University of Southern California, Los Angeles, California, USA.
[2]Department of Aeromechanics and Gas Dynamics, School of Mechanics and Mathematics, Lomonosov Moscow State University, Russia.
[3]Also at Space Research Institute (IKI) and Institute for Problems in Mechanics, Russian Academy of Sciences, Moscow, Russia.
[4]Space Environment Center, National Oceanic and Atmospheric Administration, Boulder, Colorado, USA.

0148-0227/06/2005JA011530$09.00

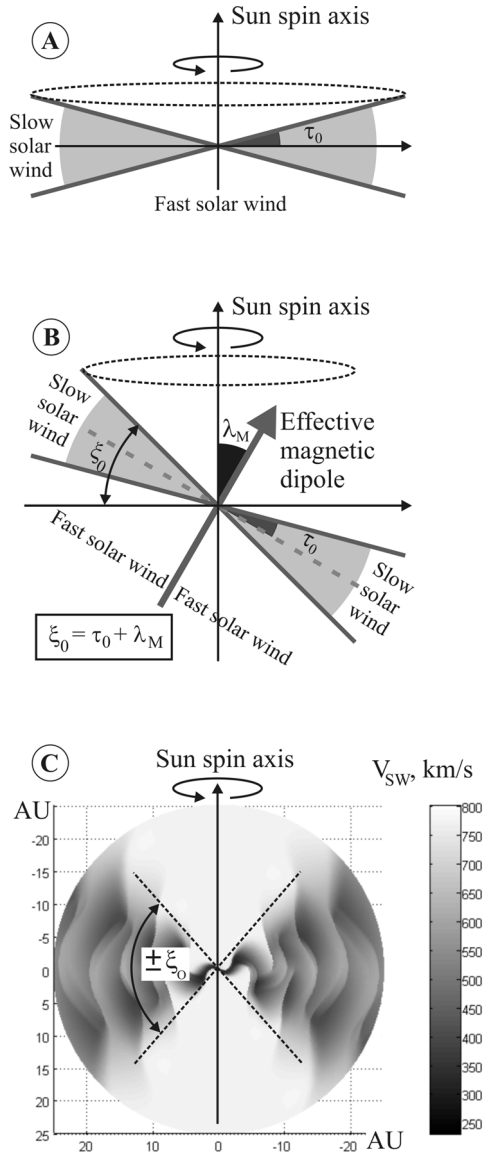

Figure 1. During solar minimum the solar wind shows pronounced anisotropy, with the velocities remarkably different in the equatorial and polar solar wind flows. (a) Simplistic model of the solar wind [*Gruntman*, 2001a], with the slow solar wind confined within the angle $\pm\tau_0$; (b) realistic solar wind (this work) with the Sun's effective magnetic dipole tilted by angle λ_M with respect to the spin axis; and (c) complex flow (velocity) field (model of *Pizzo* [1994a, 1994b]) of the realistic solar wind (Figure 1b). Note that the region within $\pm\xi_0$ is filled with mixed slow and fast plasma flows (Figures 1b and 1c).

Heliosphere imaging in EUV will likely be the next logical step in remote exploration of the galactic frontier of the solar system [*National Research Council*, 2004; *Gruntman*, 2005] after the Interstellar Boundary Explorer (IBEX) mission [*McComas et al.*, 2004] images the outer heliosphere in ENA fluxes in a few years. Scheduled for launch in 2008, IBEX will reveal the properties of the termination shock and of the solar wind proton and pickup proton populations in the heliospheric sheath [*Gruntman*, 1997; *Gruntman et al.*, 2001; *McComas et al.*, 2004].

[6] Imaging the heliosphere in EUV requires obtaining all-sky maps (angular pixels $5^\circ \times 5^\circ$) of diffuse radiation at 30.4 nm with high spectral resolution. The resolution of 0.005 nm or better would directly determine the plasma flow velocities with an accuracy of 50 km s^{-1}. In fact, the envisioned observations (from a spacecraft outside the geocorona and radiation belts) would provide a dozen or so all-sky images (maps) in spectral bins 0.005 nm wide near 30.4 nm [*Gruntman*, 2001a, 2001b; *Gruntman et al.*, 2005]. Imaging the heliosphere at this spectral range will map the heliopause; probe pickup ions in the solar wind; and reveal the three-dimensional flow pattern of the solar wind, including in the regions over the Sun's poles [*Gruntman and Fahr*, 1998; *Gruntman*, 2001a, 2001b, 2005; *Gruntman et al.*, 2005].

[7] The expected radiance of heliospheric EUV signatures is rather weak, a few milli-Rayleighs (1 mR = 10^{-3} R; 1 R = $10^6/4\pi$ phot cm^{-2} s^{-1} sr^{-1}), and its measurement presents a tough but not impossible instrumental challenge. Radiance of one milli-Rayleigh equals one photon per square centimeter in a $6.4^\circ \times 6.4^\circ$ solid angle in one second. *Gruntman et al.* [2005] and *Lampton et al.* [2005] have developed an instrumental concept to achieve the required sensitivity and spectral resolution. The enabling instrumentation is based on a Rowland-type spectrometer with multiple tall off-plane-blur-free slits of a special shape, with a large number of slits forming an aperture-coding pattern. The space mission concept and instrumentation [*Gruntman et al.*, 2005; *Lampton et al.*, 2005] are beyond the scope of this article.

[8] The first computer-simulated images of the three-dimensional solar wind flow in EUV [*Gruntman*, 2001a] were obtained for a simplistic model of the solar wind for solar minimum conditions. This original model assumed that the slow (equatorial or ecliptic) solar wind was confined within the $\tau_0 = \pm 20^\circ$ angle from the ecliptic; that the Sun effective magnetic dipole was aligned along the Sun spin axis; and that the Sun's spin axis was normal to the ecliptic plane (Figure 1a). The solar wind flow was thus axisymmetric, with the fully three-dimensional image features caused by asymmetry of the spatial distribution of atomic hydrogen (charge-exchange collision partners) of interstellar origin in the heliosphere. As a result, the simulated images of solar wind emissions exhibited a sharp boundary between the fast (polar) and slow (ecliptic) solar wind flows [*Gruntman*, 2001a, Plate 1]. Obviously two original simplifying assumptions are not valid: The Sun's spin axis is tilted by 7.25° with respect to the normal to the ecliptic plane and the angle λ_M between the Sun's effective magnetic dipole and the spin axis is essentially nonzero and could be as large as 30° (Figure 1b).

[9] The nonzero λ_M angle would result in a complex three-dimensional structure of the solar wind flow near the equator. The flow would exhibit a "wavy" pattern of density and velocity in this region and a washed out boundary between the fast and slow flows of the solar wind (Figure 1c; see also Figure 5j in section 3). The solar wind plasma with typical fast (750 km s^{-1}) and slow (450 km s^{-1}) velocities covers 10.8 and 6.5 AU, respectively, during one full rotation of the Sun (~24.9 days). Solar wind

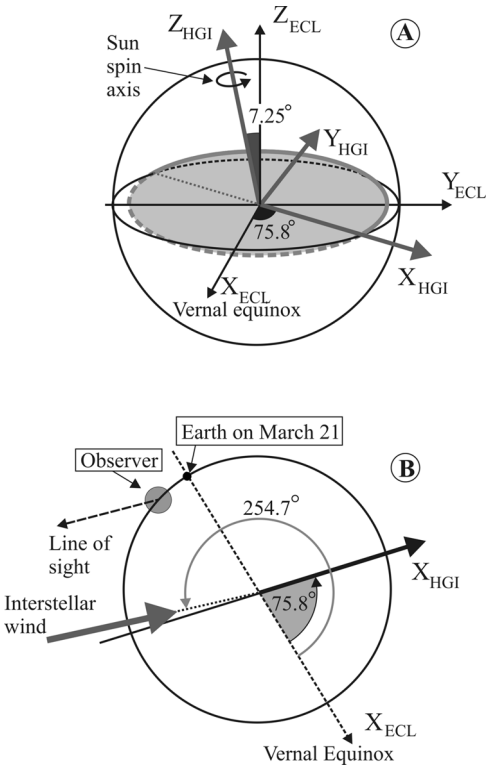

Figure 2. (a) Definition of the heliographic inertial coordinate system (HGI) with respect to ecliptic coordinates (ECL). The X_{HGI}-axis points along the intersection line of the ecliptic and solar equatorial planes. The Sun spin axis (Z_{HGI}) is tilted 7.25° with respect to the normal to the ecliptic plane (Z_{ECL}). (b) Ecliptic plane with the X_{HGI}-axis and the projection on the ecliptic plane of the interstellar wind vector. The interstellar wind comes from the direction with ecliptic latitude 5.2° and longitude 254.7°, so its vector points in the direction with latitude −5.2° and longitude 74.7°. Note that the interstellar wind direction is slightly (1.1°) off the X_{HGI}-axis. Also shown are the projections on the ecliptic plane of the observation point used in this work and the lines of sight.

imaging is line-of-sight observations with the regions producing the observed radiance, the ''source function,'' stretching from the Sun for 10 AU and more [*Gruntman*, 2001a] (see also section 3 below). The radiance measured by an observer in a given direction near the ecliptic would thus include emissions of the solar wind plasmas that originated at different heliomagnetic latitudes, with the slow and fast solar wind plasmas interacting in a complex way (Figure 1c).

[10] The question of importance for imaging of the heliosphere in EUV is whether global images (maps) with high spectral resolution would reveal the boundary between the fast and slow solar wind velocities in a realistic complex flow. Here, there are two distinct possibilities with the observations either resolving angles τ_0 and λ_M or not. In one case, imaging would determine (1) the angle $\pm\tau_0$ confining the slow solar wind; (2) the angle λ_M between the Sun's effective magnetic dipole and the spin axis; and (3) typical velocities of slow and fast plasma flows (Figure 1b). In the alternative case, the boundary between fast and slow flows would be washed out in observations near the equator and the global maps would establish only the boundary of the broader region filled with the mixed fast and slow flows, confined by the angle $\pm\xi_0 = \pm(\lambda_M + \tau_0)$, as shown in Figures 1b and 1c.

[11] The answer to the above question is critically important to formulating the concept of the space experiment to image the global heliosphere and for determining the requirements to the space mission and instrumentation. Imaging of the heliosphere in EUV includes simultaneous mapping of the heliopause and probing of the three-dimensional solar wind flow pattern [*Gruntman*, 2001a, 2001b]. If a realistic complex flow pattern (such as shown in Figure 1c) can be reconstructed from the images, then one would require obtaining several all-sky images during one Sun's rotation, say, one all-sky image per week. If, alternatively, only a boundary of the broader region ($\pm\xi_0$) filled with the mixed slow and fast flows can be obtained, then the all-sky images can average over several Sun's rotations. Therefore these two distinct cases would translate into the requirements of one image per week and a few images per year, respectively. (We note that mapping of the heliopause, achieved simultaneously with imaging of the solar wind, would require one or two all-sky images each year [*Gruntman*, 2001a, 2001b; *Gruntman et al.*, 2005].) The full sky (4π sr) contains about 1600 5° × 5° angular (directional) pixels. Therefore the two cases above would correspond to accumulation time 400 s and 10,000–20,000 s per pixel, respectively.

[12] The goal of this article is to build on the original concept of the heliosphere EUV imaging [*Gruntman*, 2001a, 2001b] and to make the next step in characterizing expected EUV signatures of the three-dimensional heliosphere and to further define the experimental concept under assumptions of a realistic truly three-dimensional solar wind flow.

2. Model

[13] We use the heliographic inertial coordinate system (HGI), which is a natural coordinate system for description of the solar wind flow. The system reference vector Z_{HGI} (the vector of the Sun's rotation) is normal to the solar equator and tilted 7.25° with respect to the normal to the ecliptic plane. The X_{HGI}-axis is directed along the intersection line of the ecliptic and solar equatorial planes; ecliptic longitude of the Sun's ascending node is 75.77° (J2000). The Y_{HGI}-axis completes the right-handed set. Heliographic latitude varies from −90° at the south pole to +90° at the north pole and longitude is counted from the X_{HGI}-axis from 0–360°. Figure 2a shows the HGI coordinate system with respect to the ecliptic coordinate system. The ecliptic plane with the X_{HGI}-axis and the projection of the interstellar wind vector are shown in Figure 2b.

[14] Solar wind EUV emissions are produced by charge exchange of the solar wind alpha particles. The surrounding local interstellar medium (LISM) moves with respect to the Sun (the interstellar wind) with the velocity ~26 km s^{-1}. Interstellar hydrogen atoms penetrate the solar system and fill the heliosphere, providing charge-exchange collision partners. (Note that heliospheric hydrogen energetic neutral atoms (ENAs) significantly contribute to the population of

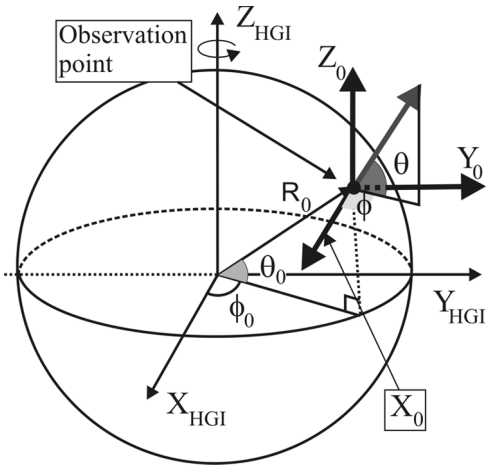

Figure 3. Observer is at (R_0, θ_0, φ_0), θ_0 and φ_0 being heliographic latitude and longitude. The axes X_0, Y_0, and Z_0 of the system of coordinates fixed with the observer are parallel to the X_{HGI}, Y_{HGI}, and Z_{HGI} axes, respectively. The direction of observation (line of site) is characterized by two angles, θ and φ, that are defined similarly to heliographic latitude θ_0 and longitude φ_0.

atomic hydrogen within 1 AU [*Gruntman and Izmodenov*, 2004]. We disregard the ENA source in this work.) The direction (latitude and longitude) from where the interstellar wind comes from is well established: 5.2° and 254.7° in ecliptic coordinates [*Witte*, 2004; *Gloeckler et al.*, 2004; *Lallement et al.*, 2005; *Moebius et al.*, 2004; *Vallerga et al.*, 2004] or 5.0° and 178.3° in HGI. The wind velocity vector thus points in the direction with latitude and longitude −5.2° and 74.7°, respectively, in ecliptic coordinates and −5.0° and −1.7°, respectively, in heliographic coordinates. Note that the interstellar wind vector is close to the line of intersection of the ecliptic plane and the solar equator (the X_{HGI} axis).

[15] The 30.4-nm radiance F (photons cm^{-2} s^{-1} sr^{-1}) at an observation point O is an integral over the line of sight $\vec{s}$

$$F = \frac{1}{4\pi} \int_{\text{Point O}}^{\infty} \alpha(\text{s})\, ds, \tag{1}$$

where $\alpha(s)$ is the rate of (assumed isotropic) emission of photons in a unit time at a point s [*Gruntman*, 2001a]. The emission rate $\alpha(s)$ at a given point $s = s(R, \theta, \phi)$ is equal to

$$\alpha(s) = \alpha(R,\theta,\phi) = n_{He^{2+}}(R,\theta,\phi) V_{SW}(R,\theta,\phi)\ n_H(R,\theta,\phi)\, \sigma_{30.4}(u), \tag{2}$$

where $n_{He^{2+}}$ and V_{SW} are the local solar wind alpha particle number density and velocity, respectively; n_H is the local number density of hydrogen atoms; $\sigma_{30.4}(u)$ is the velocity-dependent cross section to produce a 30-4-nm photon in a He^{2+}–H collision with a relative velocity u; and R is the heliocentric distance (radius). Figure 3 shows the definition of heliographic latitude and longitude.

[16] The velocity of interstellar hydrogen atoms inside the heliosphere is much smaller than the velocity of the solar wind, so we assume that the collision velocity is always equal to that of the solar wind, $u = V_{SW}$. The cross section $\sigma_{30.4}(u)$ roughly linearly increases with the collision velocity in the 300–800 km s^{-1} range [*Gruntman*, 2001a], and it can be approximated as

$$\sigma_{30.4}(u) = 1.41 \times 10^{-18} \times u - 4.3 \times 10^{-16},$$

where the collision velocity u is in km s^{-1} and the cross section $\sigma_{30.4}$ is in cm^2. Alpha-particle abundances vary in the solar wind with time and direction [e.g., *Bochsler*, 1998]. We discussed these variations as well as particle streaming elsewhere [*Gruntman*, 2001a]. In this work, we assume that alpha particles constitute 4.5% of the solar wind ion number density. We note that expected variations of the abundances of alpha particles will actually increase the contrast of images [*Gruntman*, 2001a].

[17] The velocities of alpha particles in the solar wind plasma associated with the propagating corotating interaction regions and coronal mass ejections (CMEs) may have significant nonradial and thermal components. Higher particle velocities will increase emission probabilities because of the higher charge exchange cross sections. Nonradial velocity components will result in reduced Doppler shifts of the observed radiation. The region with such alpha particles would be limited in size and its contribution will likely be small compared to the emissions of the solar wind plasma along the line of sight. Whether imaging of the solar wind is sensitive to transient structures in the solar wind, such as CMEs, is an open question [*Gruntman*, 2001a], and this subject is beyond the scope of the present study.

[18] We assume that the solar wind flow is axisymmetric with respect to the effective solar magnetic dipole. This dipole is tilted with respect to the Sun spin axis by an angle λ_M, with the slow solar wind confined within the angle $\pm\tau_0$ from the magnetic equator (Figure 1b). Our tilted-dipole model describes the spatial evolution of a steady (in a frame rotating with the Sun), three-dimensional magnetohydrodynamic (MHD) solar wind where the solution is built up over a range of heliocentric distances by outward integration of the mass, momentum, energy, and magnetic flux conservation equations in spherical shells. The details of the model assumptions and implementation are given by *Pizzo* [1982, 1994a, 1994b].

[19] Over the magnetic poles, the solar wind plasma is relatively fast, hot, and tenuous. At the magnetic equator, it is relatively slow, cold, and dense. At the inner computational boundary of 0.15 AU, we adopt the polar solar wind velocity 530 km s^{-1}. This velocity corresponds to a velocity of 760 km s^{-1} and number density 2 cm^{-3} at 1 AU. The slow solar wind with the velocity 230 km s^{-1} is confined to $\pm\tau_0 = \pm 15°$ at the inner boundary. At 1 AU, the slow solar wind would be characterized by the velocity 320 km s^{-1} and number density 10.5 cm^{-3}. (The detailed conditions at the inner computational boundary are shown in Figures 5a and 5c in section 3.) In this work, we assume the dipole tilt angle $\lambda_M = 30°$. The solar wind flow is simulated up to the 25-AU distance. A "side view" of the resulting complex flow pattern is shown in Figures 1c and 5j. The region with the mixed fast and slow solar wind flows is thus confined within $\pm\xi_0 = \pm(\lambda_M + \tau_0) = \pm 45°$. Only a few percent of the

expected photon fluxes (that reach an observer at 1 AU) originate beyond 25 AU, so we disregarded the contribution of those distant regions in this work.

[20] Interstellar hydrogen number density distribution in the heliosphere was calculated using the hot model [e.g., *Fahr*, 1974; *Holzer*, 1977; *Meier*, 1977]. This computationally convenient model does not include important plasma-gas coupling in the heliospheric interface which modifies the properties of the inflowing interstellar hydrogen [e.g., *Izmodenov et al.*, 2001]. The hot model can be reliably used however for many applications if one accounts for the interface effect by "adjusting" the velocity and temperature of the inflowing interstellar gas [*Gruntman*, 1994]. The adjusted parameters are inferred from observations at 1 AU of heliospheric hydrogen [e.g., *Costa et al.*, 1999]. Such an approximation is adequate for the purposes of the present work focused on sorting out the importance of relevant physical processes and establishing main properties of heliosphere images in EUV. The following (adjusted) interstellar atomic hydrogen parameters are used in this work: number density $n_0 = 0.14$ cm^{-3}; temperature 12000 K; bulk velocity 20 km s^{-1}; radiation-to-gravitation force ratio 0.8; and ionization rate 6.0×10^{-7} s^{-1} at 1 AU. The ionization rate is assumed inversely proportional to the square of the distance from the Sun and independent of ecliptic latitude and longitude.

3. Results and Discussion

[21] We simulate global heliospheric images for an observer at a point

$$(R_0, \theta_0, \phi_0) = (1 \text{ AU}, \ 0^\circ, \ 120^\circ)$$

in heliographic coordinates; ecliptic latitude and longitude are 6.3° and 196.0°, respectively (Figure 2b). This observation point is at the solar equator (and consequently close to the ecliptic plane) and roughly 60° from the upwind (interstellar wind) direction. The observation point is purposefully selected at a location that would show asymmetries caused by both the interstellar wind (distribution of atomic hydrogen in the heliosphere) and the solar wind flow.

[22] Figure 4 shows solar wind conditions and radiation properties along two representative lines of sight, one (left column) for the direction $\theta_1 = 0$ and $\phi_1 = 178.3^\circ$ and the other (right column) for $\theta_2 = 60^\circ$ and $\phi_2 = 178.3^\circ$. Line of sight directions are characterized by two angles, the "latitudinal" angle θ varying from -90° to $+90^\circ$ and the "longitudinal" angle ϕ from 0° to 360°. The axes X_0, Y_0 and Z_0 of the coordinate system fixed with the observer point in the directions parallel to the X_{HGI}, Y_{HGI}, and Z_{HGI} axes, respectively (Figure 3). The angle θ is counted from the plane normal to the Z_0 (Z_{HGI}) axis and the longitudinal angle ϕ is counted from the X_0 axis.

[23] We will call these two selected directions "1" and "2," respectively. While both directions point away from the Sun, the entire line of sight in direction 1 is in the solar equatorial plane and thus in the region of the "ecliptic solar wind" with the mixed slow and fast flows. It is close to the upwind (interstellar wind) direction (Figure 2b). Direction 2 points 60° off the solar equator plane and consequently the line of sight is predominantly in the fast polar solar wind.

[24] The local emission rate in a given point is a product of the local atomic hydrogen number density, solar wind number density, solar wind velocity, and velocity-dependent charge-exchange cross section (equation (2)). These parameters are shown in Figures 4a–4c for two selected lines of sight. The number densities of heliospheric atomic hydrogen (normalized to the number density n_0 "at infinity" in interstellar medium) smoothly increase with the increasing heliocentric distance along the lines of sight, reaching 80–85% (at 25 AU) of the number density in the LISM (Figure 4a). The dependences of solar wind number densities and velocities are essentially different for two selected observational directions (Figure 4b). Both the number density and velocity vary significantly along direction 1 in the equatorial solar wind, going through the regions with high and low densities and velocities. In contrast, the dependences are smooth along direction 2 when the line of sight enters the region of high-speed solar wind at $s > 1$ AU. The charge exchange cross section between alpha particles and atomic hydrogen is velocity dependent, and Figure 4c shows the cross sections corresponding to the local solar wind velocities along the lines of sight.

[25] Figure 4d shows the variation of the solar wind emission rate $\alpha(s)$ (in mR/AU) along the lines of sight. The radiance reaching the observer is an integral of the emission rate along the line of sight (equation (1)) or the area under the curves in Figure 4d. These curves are the source functions for the observed radiances. For direction 1, one can see that the maxima of solar wind 30.4-nm emissions are associated with the maxima of the solar wind number density and velocity. The maxima correspond to the areas where the line of sight crosses the corotation interaction regions (CIRs) in the solar wind.

[26] The situation is quite different for direction 2 with the line of sight out of the ecliptic plane. Roughly at s = 1 AU, the line of sight leaves the slow ($\sim$400 km s^{-1}) solar wind region. The contribution of the slow solar wind to the total radiance is clearly insignificant (the short-wavelength peak in Figure 4e, right) for this direction. The region with the high solar wind velocity (polar solar wind) and correspondingly with a large charge exchange cross section would account for most of solar wind emissions (the long-wavelength Doppler-shifted peak in Figure 4e, right) for this direction.

[27] Figure 4e shows the expected spectral radiance from the selected directions, integrated over 0.005-nm bins. In addition to wavelength, we show the corresponding (Doppler shift) velocity of emitting ions along the X axis. One can see that spectral radiance obtained for direction 2 allows clear determination of the velocity of the solar wind in polar regions. Spectral radiance for direction 1 is spread over several spectral bins resulting from a complex flow along the line of site crossing the regions with slow and fast velocities.

[28] Figure 4d also clearly shows that the regions contributing most to the observed radiance stretch up to 10 AU and beyond. We note that that both directions 1 and 2 point in the upwind (with respect to the interstellar wind) hemisphere. Observational directions in the downwind hemi-

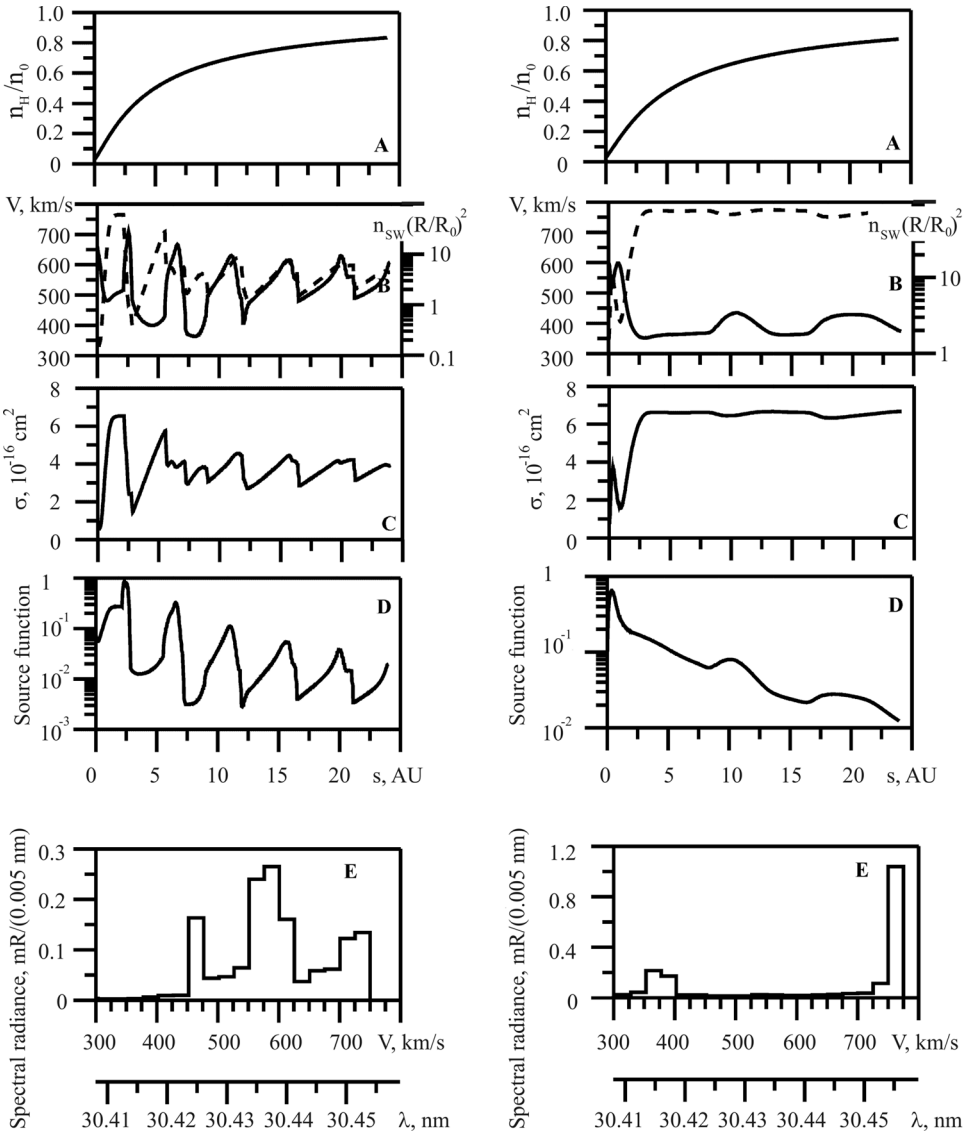

Figure 4. Properties of the solar wind and expected radiance for two directions (θ, φ): (left) (0°, 178.3°); (right) (60°, 178.3°); the observer is at (R_0, θ_0, ϕ_0) = (1 AU, 0°, 120°]. Dependences along the line of site *s*: (a) neutral atomic hydrogen number density (normalized to its value n_0 at "infinity"); (b) normalized solar wind number density n_{SW} $(R/R_0)^2$ (solid lines) and solar wind velocity (dashed lines); (c) velocity-dependent charge-exchange cross section; and (d) emission rate or the source function (mR/AU) for the radiance reaching the observer. (e) Spectral radiance summed up over 0.005-nm bins; also shown are the corresponding (Doppler shift) flow velocities along the horizontal axes.

sphere would cross the region with a significantly lower number density of heliospheric atomic hydrogen and the distances up to 20 AU or even more would significantly contribute to observed radiance. The solar wind plasma flow with typical fast and slow velocities covers roughly 11 and 6 AU, respectively, during one full rotation of the Sun. Therefore emissions contributing to observed radiance would be produced by the solar wind plasma originating during one-to-four solar rotations, depending on the particular line of sight.

[29] Figure 5 shows the three-dimensional properties of the solar wind flow and the resulting simulated all-sky images. The images are presented in the Mercator projection. For the selected observation point, the Sun is at (θ, φ) = (0, 300°) in the images (arrows in Figures 5e, 5f, 5g, and 2h). Figures 5a and 5c show solar wind flow properties (all latitudes and longitudes) at the inner computational boundary R = 0.15 AU. The solar wind velocity (in km s^{-1}) in shown in Figure 5a and the normalized number density, or $n_{SW} \times (R/R_0)^2$, in cm^{-3} is shown in Figure 5c. One can clearly see the effect of the rotation of the Sun's effective magnetic dipole, with the dipole tilt axis $\lambda_M = 30°$ and the slow solar wind confined within $\pm\tau_0 = \pm 15°$. The solar wind flow pattern is largely preserved at 1 AU. Figures 5b and 5d show the solar wind velocity and normalized number density, respectively, at 1 AU. Note that the initial (at 0.15 AU) sharp boundary between the fast and slow solar wind gradually evolves.

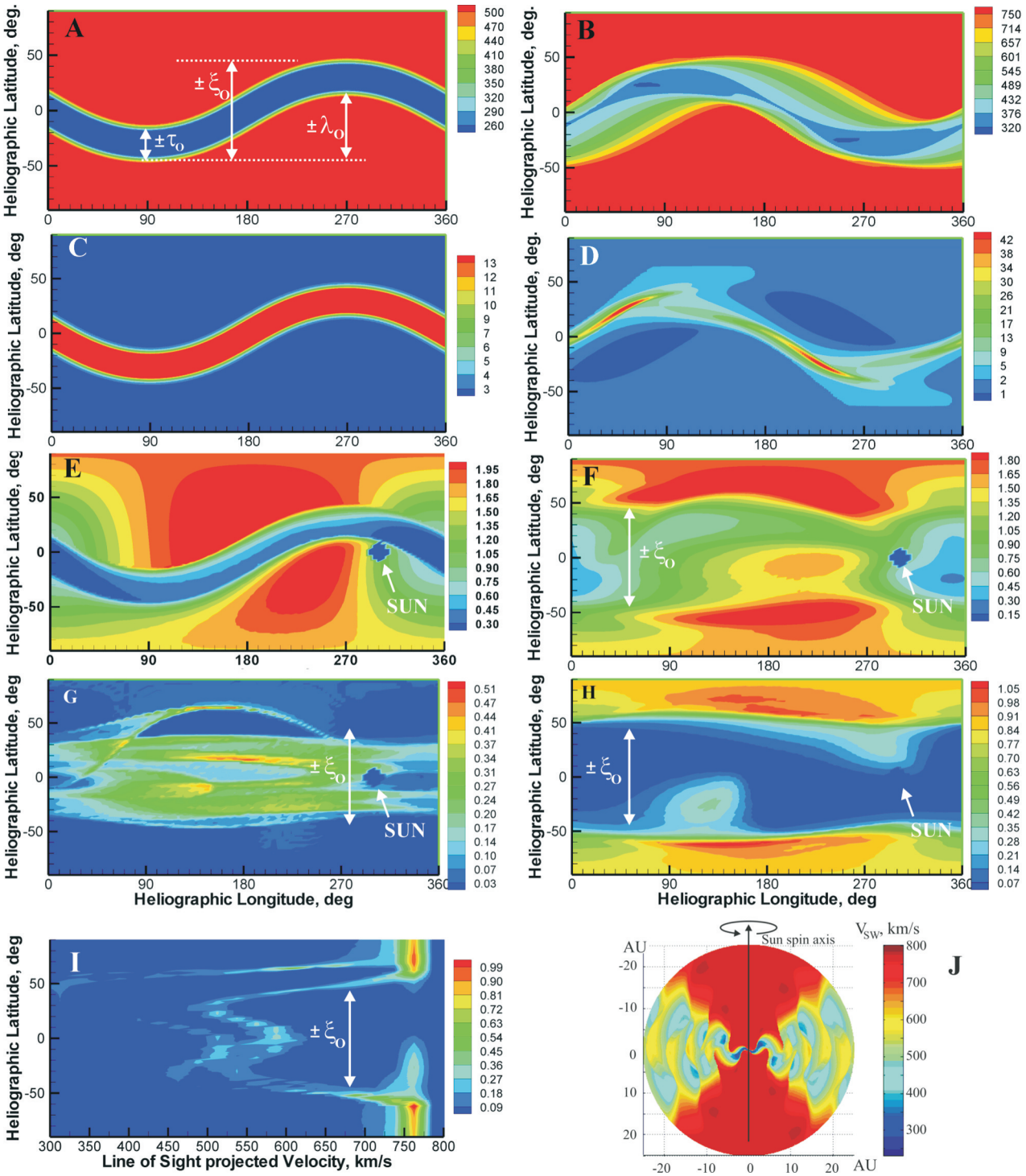

Figure 5. Solar wind flow properties (all latitudes and longitudes) at (a, c) the inner computational boundary R = 0.15 AU and at (b, d) 1 AU: Figures 5a and 5b show solar wind normalized number density $N_{SW} \times (R/R_0)^2$ (in cm^{-3}); Figures 5c and 5d show solar wind velocity V_{SW} (in km s^{-1}). All-sky maps (Mercator projection) in total solar wind emissions (milli-Rayleigh) for (e) a simplified case of $\lambda_M = 0$ and (f) a realistic case of the tilted $\lambda_M = 30°$ effective solar dipole. All-sky maps of the solar wind emissions in two (roughly 0.005-nm wide) spectral bins corresponding to (g) slow ($500 < V_{SW} < 550$ km s^{-1}) and (h) fast ($750 < V_{SW} < 800$ km s^{-1}) solar wind. The arrows in Figures 5e–5h show the vicinity of the Sun as several blackened pixels. (i) Spectral radiance for a swath in the sky (latitudes from −90° to +90°) in the direction $\phi = 120°$, with the corresponding (Doppler shift) velocity shown along the horizontal axis. (j) Color representation of Figure 1c.

[30] Figures 5e and 5f show all-sky maps of total radiance produced by the solar wind charge-exchange emissions. Figure 5e corresponds to a simplistic case with the effective Sun's magnetic dipole aligned along the Sun's spin axis, that is $\lambda_M = 0$. (This was the assumption in the original work by *Gruntman* [2001a].) The all-sky map shows a clear boundary between the fast and slow solar wind velocities in this case, with the directions primarily in the high-velocity solar wind standing out in brightness. Both, the tilt of the effective magnetic dipole λ_M and the region containing the low-velocity solar wind $\pm\tau_0$ can be obtained from such an image.

[31] Figure 5f illustrates a case of a realistic solar wind with the tilted magnetic dipole. The tilt of the magnetic dipole causes the north-south asymmetry although it manifests in a more complex way in contrast to the simple zero-tilt case shown in Figure 5e. The upwind direction with the higher atomic hydrogen number densities corresponds to longitudinal angles ϕ in the 90–270° range. Consequently, the directions with such longitudes are much brighter, as expected. Clearly, one cannot now separate the contributions of the dipole tilt (λ_M) and of the latitude range (τ_0) of the slow solar wind from an image in Figure 5f. The sum of these two effects, however, the angle $\xi_0 = \lambda_M + \tau_0$, can be obtained from such an all-sky map.

[32] Note that the shown simulated sky maps (Figure 5f) is a "snapshot" at a certain moment of time. In reality it will take a certain time (at least a week [*Gruntman et al.*, 2005]) to obtain an all-sky image, further significantly complicating extraction of the flow pattern near the equator. Therefore obtaining the exact flow pattern of the complex flow near the equator with the mixture of regions with fast and slow flows seems to be very difficult if not impossible from global heliospheric images. In contrast, if the map accumulation takes a few Sun rotations, than one can expect that the image would show a broad band ($\pm\xi_0$ wide) of relatively low brightness centered on the equator and two high-latitude bands of relatively bright polar regions. From such an image one should be able to determine the angle ξ_0 in a straightforward way.

[33] Heliosphere imaging in EUV with high spectral resolution [*Gruntman et al.*, 2005] would produce sky maps covering the spectral band corresponding to Doppler-shifted velocities in the 300–800 km s^{-1} range. The nominal width of spectral bins is 0.005 nm which roughly corresponds to the velocity bins of 50 km s^{-1}. Two examples of such maps, one for a relatively slow solar wind (velocity $500 < V_{SW} < 550$ km s^{-1}) and the other for a relatively fast solar wind (velocity $750 < V_{SW} < 800$ km s^{-1}) are shown in Figures 5g and 5h, respectively. The regions with the slow solar wind are close to the equator (Figure 5g) and would exhibit a complex rapidly changing in time pattern. In contrast, the regions with the high velocity solar wind would be pronounced and stable near the polar regions, with temporal changes occurring only near the boundary ($\pm\xi_0$) of the high-velocity region.

[34] The simulated all-sky maps clearly show that it would be very difficult if not impossible to reconstruct the exact flow pattern in the near-equatorial region. In addition, accumulation of a all-sky image would require at least 1 week [*Gruntman et al.*, 2005], washing out many features. Therefore a realistic experiment will not be able to separate the contributions of the dipole tilt (λ_M) and of the latitude range (τ_0) of the slow solar wind. Determining the sum of these two effects, however, the angle $\xi_0 = \lambda_M + \tau_0$, is possible even from all-sky images obtained over a period of several rotations of the Sun. Consequently, a space experiment should realistically focus on measuring the angle ξ_0 and require obtaining a few all-sky images per year. This latter requirement is consistent with another goal of heliosphere EUV imaging, mapping of the heliopause [*Gruntman*, 2001a, 2001b; *Gruntman et al.*, 2005].

[35] The global conditions of the three-dimensional solar wind can be inferred, however, more frequently. The local conditions in the antisolar direction from the Earth, that is corresponding to a given heliographic longitude, can be determined perhaps in a day or two. Instead of measuring all-sky images, one can require obtaining an image of the one-pixel wide (or a few-pixel wide) swath in the sky, from south to north, in the antisolar direction. Figure 5i shows spectral radiance for such a swath in the sky in the antisolar direction. Such an image can be obtained with high spectral resolution perhaps in a day or two [*Gruntman et al.*, 2005]. In addition, the instrument boresight will always be pointed at least 90° from the direction toward the Sun, thus significantly simplifying the baffle system. The horizontal axis (Figure 5i) shows the corresponding Doppler-shifted velocities. Therefore one can monitor the solar wind velocities on the daily basis. Since the Sun rotates, such one-dimensional observations during one rotation of the Sun (~27 days as observed from the Earth moving around the Sun) would allow inferring of the three-dimensional flow field of the solar wind in the heliosphere.

[36] **Acknowledgments.** This work was supported by a NASA grant. V. I. is also partly supported by RFBR grant 04-02-16559, and Program of Basic Research of OEMMPU, the Russian Academy of Sciences.

[37] Shadia Rifai Habbal thanks Stan Grzedzielski and Vladimir Baranov for their assistance in evaluating this paper.

References

Bochsler, P. (1998), Structure of the solar wind and compositional variations, *Space Sci. Rev.*, *85*, 291–302.

Costa, J., R. Lallement, E. Quémerais, J.-L. Bertaux, E. Kyrölä, and W. Schmidt (1999), Heliospheric interstellar H temperature from SOHO/SWAN H cell data, *Astron. Astrophys.*, *349*, 660–672.

Fahr, H. J. (1974), The extraterrestrial UV-background and the nearby interstellar medium, *Space Sci. Rev.*, *15*, 483–540.

Gloeckler, G., et al. (2004), Observations of the helium focusing cone with pickup ions, *Astron. Astrophys.*, *426*, 845–854.

Gruntman, M. A. (1994), Neutral solar wind properties: Advance warning of major geomagnetic storms, *J. Geophys. Res.*, *99*, 19,213–19,227.

Gruntman, M. (1997), Imaging of space plasmas in energetic neutral atom fluxes, *Rev. Sci. Instrum.*, *68*, 3617–3656.

Gruntman, M. (2001a), Imaging the three-dimensional solar wind, *J. Geophys. Res.*, *106*, 8205–8216.

Gruntman, M. (2001b), Mapping the heliopause in EUV, in *The Outer Heliosphere: The Next Frontiers*: *Proceedings of the COSPAR Colloquium*, pp. 263–271, Elsevier, New York.

Gruntman, M. (2005), Solar system frontier: Exploring the heliospheric interface from 1 AU, in *Missions to the Outer Solar System and Beyond*: *Proceedings of the Fourth IAA Symposium on Realistic Near-Term Advanced Scientific Space Missions*, edited by G. Genta, pp. 47–52, Int. Acad. of Astronaut., Aosta, Italy.

Gruntman, M. A., and H. J. Fahr (1998), Access to the heliospheric boundary: EUV echoes from the heliopause, *Geophys. Res. Lett.*, *25*, 1261–1264.

Gruntman, M., and V. Izmodenov (2004), Mass transport in the heliosphere by energetic neutral atoms, *J. Geophys. Res.*, *109*, A12108, doi:10.1029/2004JA010727.

Gruntman, M., E. C. Roelof, D. G. Mitchell, H. J. Fahr, H. O. Funsten, and D. J. McComas (2001), Energetic neutral atom imaging of the heliospheric boundary region, *J. Geophys. Res.*, *106*, 15,767–15,781.

Gruntman, M., M. Lampton, and J. Edelstein (2005), Imaging three-dimensional heliosphere in EUV, in *Solar Physics and Space Weather Instrumentation*, edited by S. Fineschi and R. A. Viereck, *Proc. SPIE Int. Soc. Opt. Eng.*, *SPIE-5901-3*.

Holzer, T. E. (1977), Neutral hydrogen in interplanetary space, *Rev. Geophys.*, *15*, 467–490.

Izmodenov, V. V., M. Gruntman, and Y. G. Malama (2001), Interstellar hydrogen atom distribution function in the outer heliosphere, *J. Geophys. Res.*, *106*, 10,681–10,690.

Lallement, R., E. Quémerais, J. L. Bertaux, S. Ferron, D. Koutroumpa, and R. Pellinen (2005), Deflection of the interstellar neutral hydrogen flow across the heliospheric interface, *Science*, *307*, 1447–1449.

Lampton, M., J. Edelstein, T. Miller, and M. Gruntman (2005), An EUV spectrometer for mapping the heliopause and solar wind, in *UV, X-Ray, and Gamma-Ray Space Instrumentation for Astronomy XIV*, edited by O. H. W. Siegmund, *Proc. SPIE Int. Soc. Opt. Eng.*, *SPIE-5898-36*.

McComas, D. J., B. L. Barraclough, H. O. Funsten, J. T. Gosling, E. Santiago-Muñoz, R. M. Skoug, B. E. Goldstein, M. Neugebauer, P. Riley, and A. Balogh (2000), Solar wind observations over Ulysses' first full polar orbit, *J. Geophys. Res.*, *105*, 10,419–10,433.

McComas, D. J., H. A. Elliott, N. A. Schwadron, J. T. Gosling, R. M. Skoug, and B. E. Goldstein (2003), The three-dimensional solar wind around solar maximum, *Geophys. Res. Lett.*, *30*(10), 1517, doi:10.1029/2003GL017136.

McComas, D., et al. (2004), The Interstellar Boundary Explorer (IBEX), in *Physics of the Outer Heliosphere*, *AIP Conf. Proc.*, vol. 719, pp. 162–181, Am. Inst. of Phys., Melville, N. Y.

Meier, R. R. (1977), Some optical and kinetic properties of the nearby interstellar gas, *Astron. Astrophys.*, *55*, 211–219.

Moebius, E., et al. (2004), Synopsis of the interstellar He parameters from combined neutral gas, pickup ion and UV scattering observations and related consequences, *Astron. Astrophys.*, *426*, 897–907.

National Research Council (2004), *Exploration of the Outer Heliosphere and the Local Interstellar Medium: A Workshop Report*, Natl. Acad. Press, Washington, D. C.

Neugebauer, M. (1999), The three-dimensional solar wind at solar activity minimum, *Rev. Geophys.*, *37*, 107–126.

Pizzo, V. J. (1982), A three-dimensional model of corotating streams in the solar wind: 3. Magnetohydrodynamic streams, *J. Geophys. Res.*, *87*, 4374–4394.

Pizzo, V. J. (1994a), Global, quasi-steady dynamics of the distant solar wind: 1. Origin of north-south flows in the outer heliosphere, *J. Geophys. Res.*, *99*, 4173–4183.

Pizzo, V. J. (1994b), Global, quasi-steady dynamics of the distant solar wind: 2. Deformation of the heliospheric current sheet, *J. Geophys. Res.*, *99*, 4185–4191.

Vallerga, J., R. Lallement, M. Lemoine, F. Dalaudier, and D. McMullin (2004), EUVE observations of the helium glow: Interstellar and solar parameters, *Astron. Astrophys.*, *426*, 855–865.

Witte, M. (2004), Kinetic parameters of interstellar neutral helium: Review of results obtained during one solar cycle with the Ulysses/GAS-instrument, *Astron. Astrophys.*, *426*, 835–844.

M. Gruntman, Astronautics and Space Technology Division, Viterbi School of Engineering, University of Southern California, 854 Downey Way, RRB-224, MC-1192, University Park, Los Angeles, CA 90089-1192, USA. (mikeg@usc.edu)

V. Izmodenov, Department of Aeromechanics and Gas Dynamics, Faculty of Mechanics and Gas Dynamics, Moscow State University, Moscow 119899, Russia. (izmod@ipmnet.ru)

V. Pizzo, Space Environment Center, NOAA, 325 Broadway, Boulder, CO 80305-3328, USA. (vic.pizzo@noaa.gov)